Two-path self-interference in PTCDA active waveguides maps the dispersion and refraction of a single waveguide mode

Schoerner, C.; Neuber, C.; Hildner, R.

Published in:
APL Photonics

DOI:
10.1063/1.5068761

APL Photonics

Two-path self-interference in PTCDA active waveguides maps the dispersion and refraction of a single waveguide mode

Cite as: APL Photonics 4, 016104 (2019); https://doi.org/10.1063/1.5068761
Submitted: 18 October 2018 . Accepted: 07 January 2019 . Published Online: 25 January 2019

C. Schörner, C. Neuber, and R. Hildner

Two-path self-interference in PTCDA active waveguides maps the dispersion and refraction of a single waveguide mode

Cite as: APL Photon. 4, 016104 (2019); doi: 10.1063/1.5068761
Submitted: 18 October 2018 • Accepted: 7 January 2019 •
Published Online: 25 January 2019

C. Schörner,[1,2] C. Neuber,[3] and R. Hildner[1,4,a)]

AFFILIATIONS

[1]Soft Matter Spectroscopy, University of Bayreuth, Universitätsstr. 30, 95440 Bayreuth, Germany
[2]Experimental Physics III, University of Bayreuth, Universitätsstr. 30, 95440 Bayreuth, Germany
[3]Macromolecular Chemistry I and Bavarian Polymer Institute (BPI), University of Bayreuth, Universitätsstr. 30, 95440 Bayreuth, Germany
[4]Zernike Institute for Advanced Materials, University of Groningen, Nijenborgh 4, 9747 AG Groningen, The Netherlands

[a)]**Electronic mail:** r.m.hildner@rug.nl

ABSTRACT

Bound waveguide modes propagating along nanostructures are of high importance since they offer low-loss energy-/signal-transport for future integrated photonic circuits. Particularly, the dispersion relation of these modes is of fundamental interest for the understanding of light propagation in waveguides as well as of light-matter interactions. However, for a bound waveguide mode, it is experimentally very challenging to determine the dispersion relation. Here, we apply a two-path interference experiment on microstructured single-mode active organic waveguides that is able to directly visualize the dispersion of the waveguide mode in energy-momentum space. Furthermore, we are able to observe the refraction of this mode at a structure edge by detecting directional interference patterns in the back-focal plane.

I. INTRODUCTION

Self-assembly of (small) organic molecules into nano- and microstructures[1] offers substantial advantages for a simple and inexpensive fabrication of novel nanophotonic devices, such as nanofibres,[2] waveguides,[3] resonators,[4] and more complex photonic circuits.[5] The overall morphology of such structures can be tailored by the chemical structure of the constituent organic molecule. For active waveguides, in which the photoluminescence (PL) of the molecules itself is guided, the specific operation wavelength can also be tuned by chemical modifications of the molecules. Moreover, such active waveguides do not require incoupling optics for the waveguided light.

In active waveguides, the propagating light can be coupled to the excitonic transitions of the constituent molecules. Such exciton-photon coupling is of great importance since it enables, for example, micron-scale energy-transport in the strong coupling regime.[6] The dispersion relation is typically used to visualise the coupling and is therefore a fundamental information required to fully characterise active waveguides. Mostly the coupling of excitons with lossy modes of microcavities,[7] lossy waveguide modes,[6,8] or localized surface plasmon resonances[9,10] is reported. Purely guided modes are often not detected since they are bound and propagate exclusively along the waveguide. For such modes, the effective mode index can be calculated by scanning the excitation spot, e.g., defined by a near-field probe,[11,12] over a sufficiently large area of the waveguide and subsequent Fourier-transform of the detected signal, which, however, is a challenging and indirect method.

Here, we show a direct approach to visualize the dispersion of guided modes in active waveguides in energy-momentum space.[13–16] We use specific microstructured waveguides that are fabricated from the perylene derivative PTCDA and support only a single bound waveguide mode due to their sub-wavelength height (56 nm). Emission from the guided mode is coupled from an edge of the waveguide to free space radiation that is detected by far-field optics.[17] This emission can be interfered with light from the spot where the waveguide mode is launched. This two-path interference between these coherent but spatially separated emission spots[18] include phase-information of the propagating waveguide mode. In contrast to our recent study focusing on the emission of organic crystals into leaky waveguide modes,[19] our approach presented here can detect the dispersion of a single bound waveguide mode in energy-momentum space. Furthermore, we demonstrate that our method is capable of visualizing the refraction process of the waveguide mode at the structure edge. Although directional emission from waveguides, e.g., plasmonic nanowires,[20] into a substrate is a known phenomenon, particularly for two-dimensional waveguide structures,[21] the relationship between the propagation direction inside the waveguide and after coupling from an edge into the substrate can differ from simple ray optics propagation. We visualize such refraction processes at nano-scale waveguide edges by directional self-interference patterns in the back-focal-plane. Our method promises to be a valuable alternative way to determine the dispersion relation of bound modes paving the way toward the observation of dynamics in waveguide mode dispersions.

II. RESULTS AND DISCUSSION

A. Structural and optical characterization of PTCDA structures

The waveguide structures investigated here are grown from perylene-3,4,9,10-tetracarboxylic dianhydride [PTCDA; see Fig. 1(a) for the chemical structure]. PTCDA is evaporated onto a glass substrate by physical vapor deposition through a shadow mask, resulting in structures with defined edges as seen by atomic force microscopy in Fig. 1(a) and by widefield photoluminescence (PL) imaging in Fig. 1(b). The height of the structures is measured to be about 56 nm and very homogeneous over the sample [Fig. 1(a)]. Using the thermal evaporation preparation approach, PTCDA forms highly ordered polycrystalline layers,[14] for which the so-called α and β crystal phases are known. In both phases, molecular packing is similar[22] with the molecular planes being preferentially parallel to the substrate and the molecules being stacked in the perpendicular direction. The close π-π stacking gives rise to strong interactions of the transition dipole moments of neighbouring PTCDA molecules, yielding delocalized (excitonic) eigenstates.[23] Hence, the optical spectra recorded from these evaporated PTCDA structures are strongly distorted compared to those of molecularly dissolved PTCDA (see Ref. 24 and Fig. S1 of the supplementary material).

From the absorption spectrum of an unstructured part of the evaporated PTCDA layer, we calculated the imaginary part of the refractive index κ; see Fig. 1(c) (blue curve). The distorted vibronic progression with a peak at 2.2 eV and a broad feature around 2.55 eV is characteristic of Frenkel excitons.[23] The in-plane real part of the refractive index n [Fig. 1(c), black curve] was determined by a singly subtractive Kramers-Kronig relation, which was shown to yield accurate results.[25] As a reference point, we used the refractive index n_r = 2.1 at a photon energy of 1.38 eV, consistent with values from the literature.[26] Below 2.1 eV, the real part of the refractive index features a clear normal dispersion. The PL spectrum of the PTCDA layer [Fig. 1(c), red curve] lacks the vibronic sub-structure and possesses a maximum at 1.73 eV, which is strongly red-shifted with respect to the absorption. We therefore attribute the PL to originate from charge-transfer and excimer emission.[14]

B. Real-space active waveguiding

To investigate the real-space waveguiding characteristics of our PTCDA structures, we performed PL imaging and spatially resolved PL spectroscopy (see Sec. IV and Ref. 19).

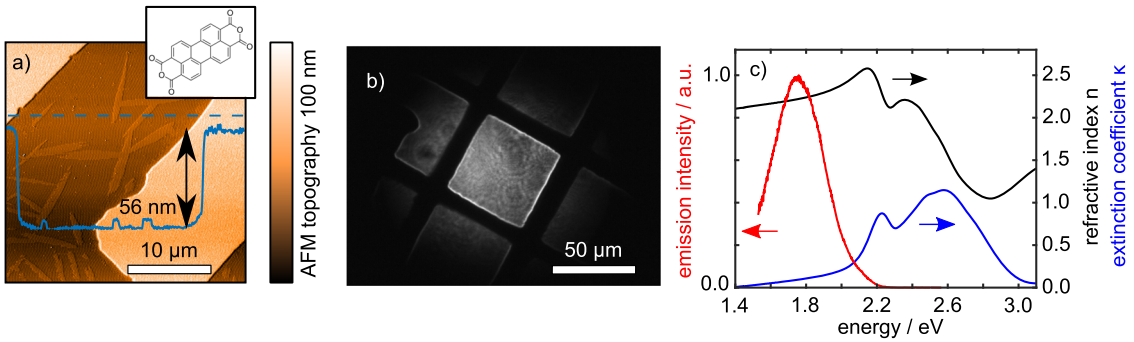

FIG. 1. (a) Atomic force microscope topography scan of a part of the PTCDA structure (molecular structure shown on top). The inset shows the height profile along the blue dashed line yielding a height of about 56 nm of the PTCDA layer. (b) Widefield photoluminescence image of a typical square PTCDA structure with a size of 50 μm. (c) The blue line shows the imaginary part of the refractive index κ (in-plane component), calculated from the measured absorption spectrum, and the black curve is the real part of the refractive index n, calculated by a Kramers-Kronig relation; see text for details. The measured photoluminescence spectrum is shown in red.

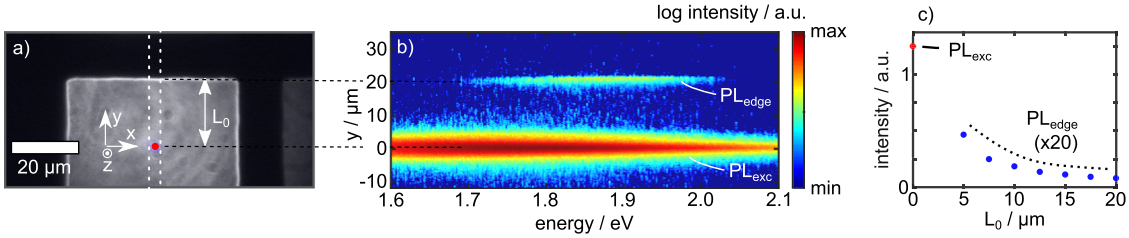

FIG. 2. (a) Widefield photoluminescence image of a PTCDA structure. The red circle displays the confocal, diffraction-limited excitation spot for the data shown in (b) and (c). (b) Photoluminescence spectra upon confocal excitation at a distance L_0 = 20 μm from the edge spatially resolved along the y-direction, which corresponds to the orientation of the spectrometer slit [dotted white lines in (a)]. (c) Spectrally integrated PL intensity at the excitation spot (PL_{exc}, red, normalized to 1) and at the edge for different L_0 (PL_{edge}, blue, multiplied by a factor of 20).

The widefield PL image of a part of a 50 μm × 50 μm structure is shown in Fig. 2(a). Since the edges appear slightly brighter than the inner part, this image provides already a clear indication for waveguiding of the PL toward the edges and subsequent coupling into the glass substrate.

Upon confocal excitation within the PTCDA structure [see Fig. 2(a), red circle] and imaging of the PL onto the vertical entrance slit of a spectrometer, we are able to measure spatially resolved PL spectra along the y-direction of the structure [see Fig. 2(a), dashed lines]. Figure 2(b) shows an example, where the structure is excited at a distance of L_0 = 20 μm from the edge. We observe a strong PL at the excitation spot and a weaker PL at the edge of the structure (note the logarithmic intensity scale). Importantly, between the excitation spot and the edge no PL is detected, indicating the guided nature of the involved waveguide mode. The PL spectra as a function of L_0 can be found in the supplementary material (Fig. S2). Here, we show in Fig. 2(c) the spectrally integrated PL intensity both at the excitation spot (PL_{exc}) and at the edge (PL_{edge}) as a function of L_0, which reveals a decreasing intensity for the PL outcoupled at the edge of the structure.

To gain deeper insights into the waveguide behavior, we performed finite-element simulations of our PTCDA structure using Comsol Multiphysics (see Sec. IV). Based on an analysis of the waveguided PL spectra that are outcoupled at the edges of the structures (see the supplementary material Fig. S2), we find that the losses, in particular, for energies below 1.85 eV, are very small. Hence, we only take into account the real part of the refractive index for the simulations of the electric near-field and neglect the imaginary part. Accordingly, the waveguide mode is a bound dielectric waveguide mode in a non-lossy medium and is determined to be the fundamental transverse-electric TE_0 mode, which is uniformly polarized in the plane [see electric field in Fig. 3(a)]. Moreover, we find that the evanescent tail penetrating the substrate medium gets larger for lower energies [see Fig. 3(a) bottom versus top]. Thus, the waveguide mode area increases for decreasing energy. This causes a lower near-field intensity at 1.7 eV [Fig. 3(b) bottom] as compared to 2.0 eV [Fig. 3(b) top] for the same total power flow along the waveguide.

Finally, we considered the outcoupling at the edge into the substrate. At 2.0 eV, we calculate that about 89% of the power is outcoupled into the substrate. The small back reflections at the edge lead to a standing wave pattern in the near-field intensity simulation in the waveguide [Fig. 3(b) top]. The modulation appears quite strong due to the non-linear relationship between electric field and intensity. As already mentioned, at 1.7 eV, the evanescent tail of the mode into the substrate get larger. Thus, the back-reflection at the edge gets weaker and nearly all power (about 96%) is outcoupled into the substrate. Note that the outcoupling of the waveguided light into the substrate occurs into a larger angular range. Thus, the outcoupled light in Fig. 3(b) top is visualized with lower intensity as inside the waveguide. In the entire considered energy range, outcoupling occurs mainly in the angular range $\theta_c < \theta < \theta_{NA}$ [see Fig. 3(b)]. Here θ_{NA} denotes the maximum collection angle of our microscope objective, and $\theta_c = \arcsin(n_{air}/n_s) \sim 41°$ is the critical angle at the substrate–air interface, with the refractive indices of air $n_{air} = 1$ and glass

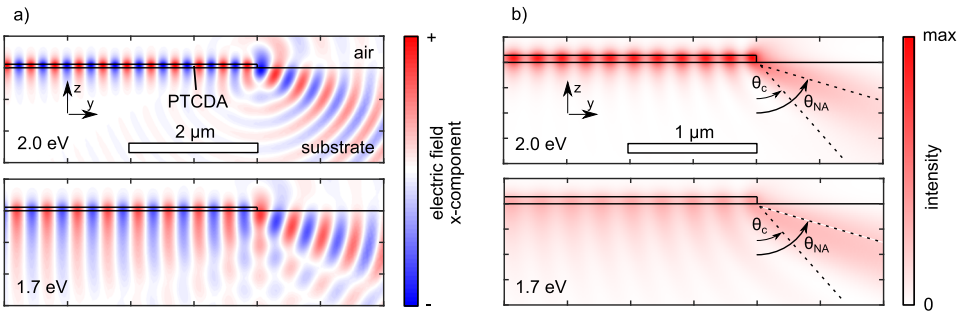

FIG. 3. (a) Simulated electric field at 2.0 eV (top) and 1.7 eV (bottom) of the TE_0 waveguide mode traveling to an edge of a 56 nm high PTCDA structure (no damping along waveguide because only the real part of the PTCDA refractive index is taken into account). (b) Simulated intensity at 2.0 eV (top) and 1.7 eV (bottom). θ_c is the critical angle at the substrate-air interface, and θ_{NA} is the maximum collection angle of the objective.

n_s = 1.51, respectively. Hence, waveguided and outcoupled PL from the edges of our structures is always detectable.

C. Mapping the dispersion relation in energy-momentum space

The directionality of the radiation characteristics of the PTCDA structures is studied by back-focal-plane (BFP) imaging as well as by energy-momentum spectroscopy (see Ref. 19 for details). Upon confocal excitation of a quadratic (50 μm × 50 μm) PTCDA structure roughly at its center, at $L_0 \sim$ 20 μm with a diffraction-limited spot, the back-focal-plane image exhibits a perfectly circular shape, as shown in Fig. 4(a). This observation shows that the PL occurs into radiation and propagating substrate modes (with $1.0 < |k_{||}|/k_0 < n_s$; k_0 magnitude of the free-space wavevector, $k_{||}$ in-plane wavevector component) independent of the in-plane ($k_x - k_y$) angle. For single crystals, a directivity in polar angles is expected due to a long-range alignment of transition dipole moments.[19] Thus, the radiation characteristics observed here is consistent with the discussed polycrystalline structure and the PL is emitted (in average) radially in the guided mode of the PTCDA layer.

Inserting a polarizer in the detection pathway with horizontal (x-) orientation, while keeping the excitation spot the same, we observe a modified back-focal-plane image with maximum PL intensity in the k_y-direction [Fig. 4(b)], which is characteristic for horizontally oriented emitting transition dipole moments. Small contributions from out-of-plane dipoles are also recognized, as reported in the literature.[14] As a function of distance L_0 between the excitation spot and edge, we observe no qualitative change in these images [Figs. 4(b)–4(f)], except for an asymmetry in the signal for $L_0 \to 0$ μm [Fig. 4(f)], which results from the presence of the nearby edge.

The corresponding energy-momentum spectra for decreasing L_0 are displayed in Figs. 4(g)–4(k). Here, the PL with $k_x \sim 0$ is imaged onto the (y-oriented) entrance slit of the spectrometer. These spectra exhibit nearly the same spectral shape for all k_y-directions. Furthermore, weak, low-contrast,

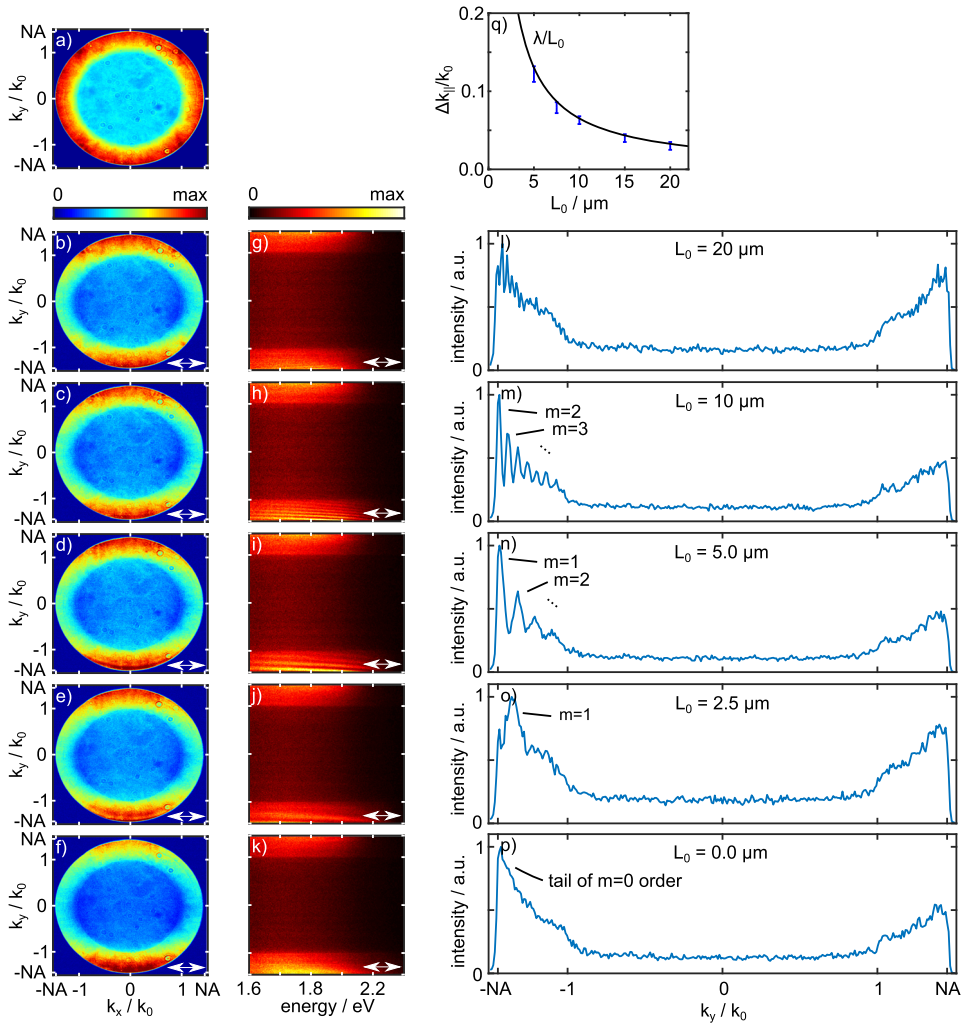

FIG. 4. (a) Unpolarized back-focal-plane image of the PL excited in the middle of a 50 μm × 50 μm PTCDA structure. [(b)–(f)] Back-focal-plane images with horizontal (x-oriented) polarizer in the detection path as a function of decreasing distance L_0 in the negative k_y-direction. [(g)–(k)] Corresponding energy-momentum spectra. [(l)–(p)] Profiles along the k_y-direction of the energy-momentum spectra at 1.9 eV. (q) Experimental fringe spacing $\Delta k_{||}/k_0$ at 1.9 eV as a function of L_0 (blue) overlaid with the dependency λ/L_0 (black, evaluated at 1.9 eV or λ = 650 nm).

high-frequency fringes appear in the negative k_y-direction [see Fig. 4(l) for a profile along the k_y-axis at a photon energy of 1.9 eV]. These fringes feature a dispersive shape with a characteristic bending toward larger $|k_y|$ for increasing energy [see, e.g., Fig. 4(i)]. Owing to this bending, the patterns are not visible in the back-focal-plane images in Figs. 4(b)–4(f), which are averaged over all energies. The fringes disappear in the energy-momentum spectrum for the vertical (y-) orientation of the polarizer because the horizontally polarized waveguide signal from the edge is blocked and the waveguided PL in the k_x-direction is suppressed by the vertical entrance slit (not shown).

Decreasing the distance L_0 between the excitation spot and the edge, we observe clear trends in those fringes [Figs. 4(l)–4(p)]: First, the contrast changes as a function of L_0 with a maximum contrast around 5-10 μm. Second, for decreasing L_0, the width and spacing of the fringes increase in k-space. The contrast decreases for shorter L_0 mainly due to the Fourier-properties of the light wave that yield an increasing full width at half maximum (FWHM Δk_{wg}) of the waveguide mode in k-space $\Delta k_{wg} \approx 1/(L_0 k_0)$ (this expression is strictly valid if L_0 is an exponential decay length[27]). Moreover, the excitation spot size becomes comparable to L_0. For large L_0, the relative signal collected at the edge of the PTCDA structure decreases [see Fig. 2(c) and Fig. S2 of the supplementary material], and the fringe spacing $\Delta k_{||}$ (see below) becomes comparable to the pixel size of the detector, which also reduces the contrast.

Analyzing the spacing $\Delta k_{||}$ between the fringes in more detail, we find from the profiles at 1.9 eV in Figs. 4(l)–4(p) that it nicely follows the relation $\Delta k_{||}/k_0 = \lambda/L_0$ [Fig. 4(q), with λ = 650 nm being the wavelength at a photon energy of 1.9 eV]. Such behavior is typical for interference between two paths with increasing difference in path lengths, as, e.g., observed in Young's double slit experiment. In analogy to our recent work,[19] we therefore consider in the following two light paths a and b [Fig. 5(a)] and calculate the phase accumulated in each of these paths: First, owing to the presence of radiation modes, the PL can be directly emitted into the substrate at the excitation spot (*path a*). Second, as demonstrated by the simulations, the PTCDA structure offers a single waveguide mode, into which the emitters will therefore radiate as well (*path b*). After guiding to the edges, the PL is (partly) coupled into the substrate mainly in the angular range $\theta > \theta_c$ which we detect until $\theta = \theta_{NA}$ [see Fig. 3(b)]. Since the emitting transition dipole moment at the excitation spot defines the phase of the two light waves, their relative phase thus depends on the distance L_0 between the excitation spot and the edge as well as the direction of the far field detection. Coherent superposition between the two paths will then result in a L_0-dependent interference pattern in k-space, as observed in Figs. 4(g)–4(k).

During propagation along *path b*, the light accumulates a phase of $k_0 n_{wg}^{eff} L_0$ in the waveguide, with n_{wg}^{eff} being the real part of the effective index of the waveguide mode. The outcoupling into the substrate at the edge is accompanied by no additional phase, as revealed by our simulations [Fig. 3(a)]. For *path a*, we have to consider the phase accumulated by the light wave during propagation to a plane perpendicular to its wavevector and containing the position, where the wave is coupled out at the egde [see Fig. 5(a)]. This phase is given by $k_{||} L_0$. In general, there will be an additional small positive phase Φ_a accumulated during the propagation of the light wave from the emitter to the substrate as determined by simulations of the multilayer geometry.[19] In our case, the thickness of the PTCDA layer of about 56 nm is much smaller than the wavelength of light and Φ_a can be neglected.

If the phases accumulated along *path a* and *path b* differ by a multiple of 2π, the condition of constructive interference of order m is fulfilled,

$$n_{wg}^{eff} k_0 L_0 - k_{||}^m L_0 = m 2\pi. \quad (1)$$

Hence, in the back-focal-plane, we get interference maxima of order m at positions $k_{||}^m$,

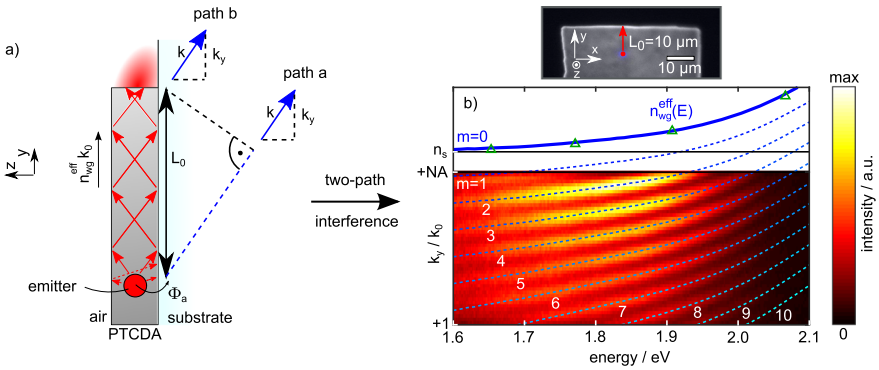

FIG. 5. (a) Side view of the geometry for two-path self-interference in active waveguides (here: PTCDA layer) where the PL of emitters is directly radiated into the substrate at the excitation spot (*path a*) and waveguided to an edge and outcoupled into the substrate (*path b*). (b) Energy-momentum spectrum of the PTCDA emission excited in a distance of L_0 = 10 μm to an edge in the positive k_y direction (confocal excitation at the red position in the top inset). Interference orders with $m \geq 2$ are observed experimentally (blue dashed line represent a fit to the theory). Extrapolation to m = 0 yields the dispersion relation of the bound waveguide mode (solid blue line). Simulated values are shown as green triangles. See text for details.

$$\frac{k_{||}^{m}}{k_0} = n_{wg}^{eff} - \frac{\lambda}{L_0} m. \quad (2)$$

We note that in this equation, the refractive index of the waveguide medium only enters indirectly in the effective waveguide mode index n_{wg}^{eff} and not in any other parameter of the equation. The 0-th order ($m = 0$) maximum in k-space is located at the position of the effective index of the waveguide mode n_{wg}^{eff}. Starting from this position, interference maxima of higher order appear with a spacing given by $\frac{\lambda}{L_0}$, reaching also the experimentally accessible range $|k_y|/k_0 < \mathrm{NA} = 1.45$.

By carefully varying the distance L_0, we can count the interference orders m corresponding to the interference fringes, as demonstrated in Figs. 4(l)–4(p). For instance, at a photon energy of 1.9 eV ($\lambda = 650$ nm), we find from our simulations $n_{wg}^{eff} = 1.57$, and the $m = 0$ interference fringe is thus located at that n_{wg}^{eff} position. Although this is slightly above the substrate refractive index ($n_s = 1.51$) and thus above the experimentally observable angular range (NA = 1.45), we observe the tail of the $m = 0$ fringe for very short distances $L_0 \rightarrow 0$ μm because the waveguide mode becomes very broad in k-space [$\Delta k_{wg} \propto 1/L_0$; see Fig. 4(p)]. For increasing L_0, the tail of the $m = 0$ fringe is pushed out of the observable range and only higher order ($m > 0$) interferences are visible [Figs. 4(m)–4(o)]. The evolution of the fringe pattern upon increasing L_0 from 0 to 10 μm is visualized in the supporting video file (see the supplementary material). Analyzing our experimental data for $L_0 = 10$ μm with Eq. (2), we obtain an energy dependent n_{wg}^{eff} in very good agreement with simulated values [see Fig. 5(b)]. We note that a surface roughness of the waveguide surface [here about 1 nm rms roughness, Fig. 1(a)] can be seen as a local variation of the waveguide's height. This induces the effective mode index to change accordingly, which will lead to small scattering losses.[28] In the simulations, we find that changing the height of the PTCDA layer by 1 nm affects the values of n_{wg}^{eff} by only less than 9×10^{-3} in the whole considered energy range, which is only a very minor effect and can thus be neglected.

Finally, we take a closer look at the dispersive shape of the interference fringes. As mentioned already, we observe a clear bending toward higher wavevectors $|k_y|$ as the energy approaches the absorption edge (at ~2.1 eV) of the PTCDA layer [see, e.g., Fig. 5(b)], which indicates interaction between the waveguide mode and the absorbing excitons. For energies between 1.6 and 1.7 eV, we observe an approach of the guided waveguide mode to cutoff as n_{wg}^{eff} becomes similar to the refractive index of the substrate $n_s = 1.51$ [black line in Fig. 5(b)]. This finding is consistent with the PL spectra detected at the edge which are cut-off toward 1.6 eV and the negligible loss coefficient above this energy (see Fig. S2 of the supplementary material).

D. Directional refraction of the waveguide mode at an edge

So far we have focused on the interference patterns along the k_y-direction in the energy-momentum spectra, where $k_x = 0$ and thus *path b* is perpendicular to the outcoupling edge. Any directional information about interference in the back-focal-plane images in Figs. 4(b)–4(f) is hidden due to the averaging over all energies. In case of directional two-path interference, the length of *path b* to a straight edge is angle dependent $L_{wg} = \frac{L_0}{\cos(\Phi_{wg})}$[$\Phi_{wg}$ is the polar angle within the waveguide; see Fig. 6(a)]. Furthermore, the phase considered for *path a* is given by $k_{||} L_p = k_{||} L_{wg} \cos(\Phi_{BFP} - \Phi_{wg})$, where Φ_{BFP} is the polar angle in the substrate medium. Hence, we get interference maxima of order m at positions $k_{||}^m$ in the back-focal plane,

$$\frac{k_{||}^{m}}{k_0} = \frac{L_{wg}}{L_p} n_{wg}^{eff} - \frac{\lambda}{L_p} m. \quad (3)$$

To visualize those interference fringes in the entire $k_x - k_y$-plane, we therefore filter the PL of PTCDA-structures in a narrow 26 meV energy band centered around 1.8 eV (corresponding to a 10 nm bandpass centered around 690 nm) and observe the self-interference in the full angular range of the back-focal plane. We have chosen the PL at 1.8 eV because it is waveguided only slightly above cutoff [see Fig. 5(b)], and we expect a large evanescent tail of the waveguide mode traveling in the substrate medium [see Figs. 3(a) and 3(b)].

Figures 6(b) and 6(c) show widefield PL images of the PTCDA structure used to visualise interference and refraction. The corresponding back-focal-plane images of the PL upon confocal excitation of this structure for different distances to the straight edge in the positive y-direction [red dots, $L_0 = 3.3$ in Fig. 6(b) and 7.0 μm in Fig. 6(c)] are displayed in Figs. 6(d) and 6(e). These back-focal-plane images feature a complex interference pattern with interesting angular dependency. In the k_y-direction ($k_x = 0$), we observe interference fringes with increasing number and decreasing spacing λ/L_0 for increasing L_0 ($\lambda = 690$ nm). The $m = 0$ interference order (solid blue line) for $k_x = 0$ is just slightly above $n_s = 1.51$, confirming that the waveguide mode is propagating slightly above cutoff.

In the polar direction starting from the k_y-direction, we observe a bending of the maxima toward higher $k_{||}$. Those directions correspond to propagation with increasing polar angle Φ_{BFP} in the substrate medium and, given the refraction at the PTCDA–air interface, also in the waveguide layer [see Fig. 6(a)]. This polar angle within the waveguide Φ_{wg} increases the phase accumulated along *path b* and gives rise to the bending of the interference fringes.

In the back-focal-plane images, we only observe the radiation angle in the substrate medium (Φ_{BFP}). Although the angles within the waveguide (Φ_{wg}) are not directly detected, the directional interference patterns allow us to obtain information about the refraction process of the waveguide mode at the edge of the PTCDA structure into the substrate medium. For perylene single crystals above cutoff, it is known that the waveguide mode can only couple out below a certain critical polar angle, determined to be about 33°, where total internal reflection sets in.[21] Here, we observe the refraction of the waveguide mode at a nano-scale edge and show that critical angles are quite different near cutoff. Thus, we relate both polar angles Φ_{wg} and Φ_{BFP} by an effective Snellius law

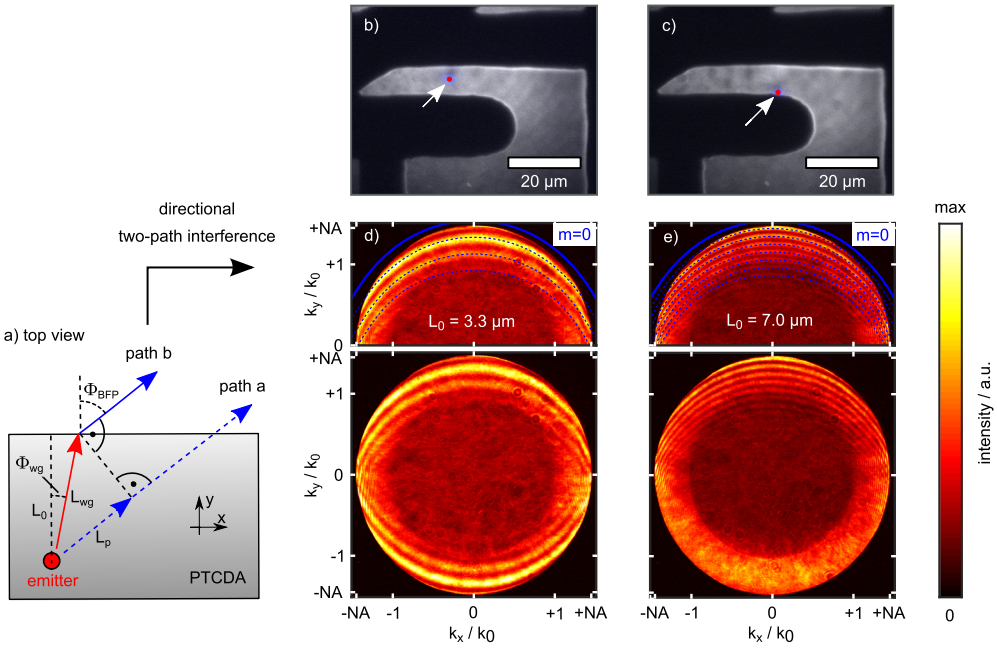

FIG. 6. (a) Top view sketch for directional two-path self-interference near a straight edge in the positive *y* direction. For details, see text. [(b) and (c)] Widefield PL images of a PTCDA structure. [(d) and (e)] Corresponding back-focal-plane images of the emission excited at the red positions in (b) and (c), and spectrally filtered to observe only at a photon energy of 1.8 eV. The blue solid (m = 0) and dashed (m > 0) lines are fits to the theory of directional self-interference.

$n_{in} \sin(\Phi_{wg}) = n_{out} \sin(\Phi_{BFP})$, where n_{out} = 1.51 is the refractive index of the substrate medium and n_{in} is fit to 1.8 ± 0.05 to match the angular trend of the interference maxima [see blue dashed lines in Figs. 6(d) and 6(e)]. The value of n_{in} is lower than expected from the refractive index of the PTCDA layer of 2.24 at 1.8 eV. We thus conclude that the refraction in the weakly guiding regime at 1.8 eV near cutoff is much weaker than expected for a PTCDA–substrate or even a PTCDA–air interface and critical angles can differ strongly from simple ray optics considerations.

In the limiting case of no refraction at the edge, all interference maxima would meet in the back-focal-plane at $|k_x|/k_0 = n_{wg}^{eff}$, $k_y = 0$ for our geometry. The small shift of the interference orders crossing the k_x-axis is thus a direct visualization of finite refraction at the structure edge. As mentioned, the high mode area near cutoff gives rise to a high outcoupling at the edge and Fabry-Perot like reflections inside the waveguide can be neglected. Therefore modulations along each interference maximum are not observed.

III. CONCLUSION

In conclusion, we have shown that thin layers of PTCDA can be applied as active single-mode waveguides operating near cutoff. In energy-momentum space, we observed interference between the PL directly from the excitation spot and the PL outcoupled from an edge of the PTCDA layer after being waveguided. This approach enabled us to monitor the dispersive character of the involved bound waveguide mode. A theoretical treatment of this self-interference allowed the determination of the absolute and energy-dependent value of the effective waveguide mode index n_{wg}^{eff}. This dispersion relation is of fundamental importance for studying light propagation and its interaction with matter. By real-space spectroscopy, we found energy-dependent waveguide losses due to reabsorption of the guided photons. Furthermore, the waveguided PL spectrum outcoupled at a PTCDA edge is modified compared to that detected directly from the excitation spot, which we attributed to energy-dependent in- and out-coupling processes into and out of the active waveguide.

We note that interference effects of the PL can be observed in real-space spectroscopy, e.g., in Fabry-Perot resonances, in one-dimensional nanofiber waveguides, and in structures supporting whispering gallery modes.[5,29,30] We do not observe such Fabry-Perot resonances in the PL of our PTCDA structure. This we attribute mainly to the two-dimensional propagation in our waveguide which effectively hinders superposition of counterpropagating waves [which, however, can be observed in the one-dimensional propagation in the simulation of Fig. 3(b)]. Furthermore, we recently observed high contrast self-interference patterns of the PL generated inside active organic waveguides with heights exceeding ~1 μm that result from multiple reflections between top and bottom interfaces of the waveguide medium.[19] This interference mechanism does not play a role in our present study due to the deep subwavelength height (56 nm) of our PTCDA layers.

Importantly, our method directly probes interference patterns in energy-momentum space, even if interference is not observed in real-space. This approach provides a fast way to visualize dispersion relations of bound modes. We envision this method to be applicable to the strong coupling regime of excitons coupled to bound waveguide modes or even to be able to detect temporal dynamics in dispersion relations. As this technique is independent of the particular (organic) system, it will be applicable to a wide variety of active waveguide materials.

IV. EXPERIMENTAL SECTION

A. Physical vapor deposition of PTCDA

For preparation of thin PTCDA films, a vapor deposition chamber (PLS 500, Balzers) was used. We attached a TEM grid as a shadow mask directly to the glass substrate to obtain the 50 μm × 50 μm squares of PTCDA. About 100 mg of PTCDA was weighted in quartz crucibles which were placed into the effusion cell (source). At 10^{-5} to 10^{-6} mbar, a constant evaporation rate was set manually to about 0.3 nm/s by slowly increasing the temperature of the effusion cells. Quartz crystal sensors were mounted near the source to measure the evaporation rate. At the final constant evaporation rate, the shutter was opened to start the deposition onto the TEM grid covered substrate. The absolute thickness of 56 nm of the PTCDA film was measured after the evaporation via atomic force microscopy (Easy Scan 2, Nanosurf), which was calibrated with a 119 nm high calibration grid (No. BT00200, Nanosurf).

B. Optical microscopy and spectroscopy

Details about the experimental setup can be found elsewhere.[19] Briefly, we used a home-built optical microscope that can be operated in confocal and widefield mode; back-focal-plane imaging and spectroscopy was performed in confocal mode with an additional Bertrand lens in the detection path. The excitation source was a diode laser (LDH-P-C-450B, Picoquant), providing pulses at a wavelength of 450 nm with a width of 60 ps and a repetition rate of 20 MHz. The PL was detected either with an imaging CCD camera (Orca-ER, Hamamatsu) or with an emCCD-camera attached to a spectrograph (SP2150i, Princeton Instruments; iXon DV887-BI, Andor). Spatially resolved PL spectroscopy was performed by detecting the emission along the spectrometer entrance slit which is oriented along the vertical y-direction [see Fig. 2(a)]. The absorbance of the PTCDA layer was measured by a commercial spectrometer (LAMBDA 750 UV/VIS/NIR, PerkinElmer) at an unstructured position (uniform height) of the layer. In the reference arm of the spectrometer, an empty substrate was inserted.

C. Simulations

The waveguide simulations are performed with Comsol multiphysics version 5.3a. The model is two-dimensional (third dimension is taken to be infinite) and surrounded by perfectly matched layers to absorb all outgoing lightwaves and avoiding reflections from the domain boundaries of the model. The geometry is given by the substrate (modeled by refractive index 1.51), a 56 nm layer of PTCDA [modeled by refractive index in Fig. 1(c)] with an abrupt edge and air (refractive index 1). The TE_0 waveguide mode is calculated by means of a boundary mode analysis of the substrate-PTCDA-air multilayer stack. The mode is launched at the left side of the model by a mode port with fixed input power. Starting from this position, the electric near-field propagating along the PTCDA waveguide and radiated from the edge is calculated by solving the Maxwell-equations in the frequency domain. Electric near-fields are calculated by taking only the real part of PTCDAs refractive index into account. The effective mode indices [Fig. 5(b)] are calculated by considering the full complex refractive index of PTCDA. The imaginary part is calculated from the absorption spectrum [Fig. 1(c)], yielding the in-plane imaginary part of the refractive index, which is the component the TE_0 waveguide mode experiences during propagation due to its in-plane polarization.

SUPPLEMENTARY MATERIAL

Supplementary material consists of a comparison of the absorption and emission of PTCDA in crystalline layer and solution and an analysis of the waveguided PL spectra. Furthermore a multimedia video file (format: mp4) provides real-time observation of the interference pattern when changing the parameter L_0 from 0 to 10 μm (Multimedia view).

ACKNOWLEDGMENTS

C.S. and R.H. gratefully acknowledge financial support from the German Research Foundation (Deutsche Forschungsgemeinschaft through Grant No. GRK1640). C.S. appreciates helpful discussions with Markus Lippitz and the opportunity of using Comsol Multiphysics. R.H. is grateful for additional support from Elitenetzwerk Bayern (ENB) *Macromolecular Science*.

REFERENCES

[1]Q. Kong, Q. Liao, Z. Xu, X. Wang, J. Yao, and H. Fu, "Epitaxial self-assembly of binary molecular components into branched nanowire heterostructures for photonic applications," J. Am. Chem. Soc. **136**, 2382–2388 (2014).

[2]L. Zang, "Interfacial donor-acceptor engineering of nanofiber materials to achieve photoconductivity and applications," Acc. Chem. Res. **48**, 2705–2714 (2015).

[3]F. Balzer, V. G. Bordo, A. C. Simonsen, and H.-G. Rubahn, "Optical waveguiding in individual nanometer-scale organic fibers," Phys. Rev. B **67**, 115408 (2003).

[4]C. Zhang, C.-L. Zou, Y. Yan, C. Wei, J.-M. Cui, F.-W. Sun, J. Yao, and Y. S. Zhao, "Self-assembled organic crystalline microrings as active whispering-gallery-mode optical resonators," Adv. Opt. Mater. **1**, 357–361 (2013).

[5]C. Zhang, Y. Yan, Y. S. Zhao, and J. Yao, "From molecular design and materials construction to organic nanophotonic devices," Acc. Chem. Res. **47**, 3448–3458 (2014).

[6]G. G. Rozenman, K. Akulov, A. Golombek, and T. Schwartz, "Long-range transport of organic exciton-polaritons revealed by ultrafast microscopy," ACS Photonics **5**, 105–110 (2018).

[7]D. G. Lidzey, D. D. C. Bradley, M. S. Skolnick, T. Virgili, S. Walker, and D. M. Whittaker, "Strong exciton-photon coupling in an organic semiconductor microcavity," Nature **395**, 53–55 (1998).
[8]K. Chevrier, J.-M. Benoit, C. Symonds, J. Paparone, J. Laverdant, and J. Bellessa, "Organic exciton in strong coupling with long-range surface plasmons and waveguided modes," ACS Photonics **5**, 80–84 (2018).
[9]R. Chikkaraddy, B. Nijs, F. Benz, S. J. Barrow, O. A. Scherman, E. Rosta, A. Demetriadou, P. Fox, O. Hess, and J. J. Baumberg, "Single-molecule strong coupling at room temperature in plasmonic nanocavities," Nature **535**, 127–130 (2016).
[10]F. Todisco, M. De Giorgi, M. Esposito, L. De Marco, A. Zizzari, M. Bianco, L. Dominici, D. Ballarini, V. Arima, G. Gigli, and D. Sanvitto, "Ultrastrong plasmon-exciton coupling by dynamic molecular aggregation," ACS Photonics **5**, 143–150 (2018).
[11]Z. Fei, M. E. Scott, D. J. Gosztola, J. J. Foley, J. Yan, D. G. Mandrus, H. Wen, P. Zhou, D. W. Zhang, Y. Sun, J. R. Guest, S. K. Gray, W. Bao, G. P. Wiederrecht, and X. Xu, "Nano-optical imaging of WSe_2 waveguide modes revealing light-exciton interactions," Phys. Rev. B **94**, 081402 (2016).
[12]F. Hu, Y. Luan, M. E. Scott, J. Yan, D. G. Mandrus, X. Xu, and Z. Fei, "Imaging exciton-polariton transport in $MoSe_2$ waveguides," Nat. Photonics **11**, 356 (2017).
[13]T. H. Taminiau, S. Karaveli, N. F. van Hulst, and R. Zia, "Quantifying the magnetic nature of light emission," Nat. Commun. **3**, 979 (2012).
[14]J. A. Schuller, S. Karaveli, T. Schiros, K. He, S. Yang, I. Kymissis, J. Shan, and R. Zia, "Orientation of luminescent excitons in layered nanomaterials," Nat. Nanotechnol. **8**, 271–276 (2013).
[15]C. M. Dodson, J. A. Kurvits, D. Li, M. Jiang, and R. Zia, "Magnetic dipole emission of Dy^{3+}:Y_2O_3 and Tm^{3+}:Y_2O_3 at near-infrared wavelengths," Opt. Mater. Express **4**, 2441 (2014).
[16]D. Li, M. Jiang, S. Cueff, C. M. Dodson, S. Karaveli, and R. Zia, "Quantifying and controlling the magnetic dipole contribution to 1.5-μm light emission in erbium-doped yttrium oxide," Phys. Rev. B **89**, 161409 (2014).
[17]S. Motamen, C. Schörner, D. Raithel, J.-P. Malval, T. Jarrosson, F. Serein-Spirau, L. Simon, R. Hildner, and G. Reiter, "Low loss optical waveguiding in large single crystals of a thiophene-based oligomer," Phys. Chem. Chem. Phys. **19**, 15980–15987 (2017).
[18]D. Wolf, T. Schumacher, and M. Lippitz, "Shaping the nonlinear near field," Nat. Commun. **7**, 10361 (2016).
[19]C. Schörner, S. Motamen, L. Simon, G. Reiter, and R. Hildner, "Self-interference of exciton emission in organic single crystals visualized by energy-momentum spectroscopy," ACS Omega **3**, 6728–6736 (2018).
[20]T. Shegai, V. D. Miljković, K. Bao, H. Xu, P. Nordlander, P. Johansson, and M. Käll, "Unidirectional broadband light emission from supported plasmonic nanowires," Nano Lett. **11**, 706–711 (2011).
[21]K. Takazawa, "Understanding the emission pattern produced by focused laser beam excitation of perylene square single crystals," Chem. Phys. Lett. **667**, 284–289 (2017).
[22]M. Möbus, N. Karl, and T. Kobayashi, "Structure of perylene-tetracarboxylic-dianhydride thin films on alkali halide crystal substrates," J. Cryst. Growth **116**, 495–504 (1992).
[23]N. J. Hestand and F. C. Spano, "Expanded theory of h- and j-molecular aggregates: The effects of vibronic coupling and intermolecular charge transfer," Chem. Rev. **118**, 7069 (2018).
[24]U. Gmez, M. Leonhardt, H. Port, and H. Wolf, "Optical properties of amorphous ultrathin films of perylene derivatives," Chem. Phys. Lett. **268**, 1–6 (1997).
[25]C. Schörner, D. Wolf, T. Schumacher, P. Bauer, M. Thelakkat, and M. Lippitz, "Nondestructive probing of a photoswitchable dithienylethene coupled to plasmonic nanostructures," J. Phys. Chem. C **121**, 16528–16532 (2017).
[26]R. Scholz, I. Vragović, A. Yu. Kobitski, M. Schreiber, H. P. Wagner, and D. R. T. Zahn, "Frenkel exciton model of low temperature photoluminescence in PTCDA single crystals," Phys. Status Solidi B **234**, 402–410 (2002).
[27]G. Colas des Francs, J. Grandidier, S. Massenot, A. Bouhelier, J.-C. Weeber, and A. Dereux, "Integrated plasmonic waveguides: A mode solver based on density of states formulation," Phys. Rev. B **80**, 115419 (2009).
[28]Y. Wang, M. Kong, Y. Xu, and Z. Zhou, "Analysis of scattering loss due to sidewall roughness in slot waveguides by variation of mode effective index," J. Opt. **20**, 025801 (2018).
[29]D. O'Carroll, I. Lieberwirth, and G. Redmond, "Microcavity effects and optically pumped lasing in single conjugated polymer nanowires," Nat. Nanotechnol. **2**, 180–184 (2007).
[30]K. Takazawa, J.-i. Inoue, K. Mitsuishi, and T. Takamasu, "Fraction of a millimeter propagation of exciton polaritons in photoexcited nanofibers of organic dye," Phys. Rev. Lett. **105**, 067401 (2010).